Materials and Design 186 (2020) 108204

Contents lists available at ScienceDirect

Materials and Design

journal homepage: www.elsevier.com/locate/matdes

Precipitation in an extruded AA7003 aluminium alloy: Observations of 6xxx-type hardening phases

A. Lervik[a,*], C.D. Marioara[b], M. Kadanik[d,e], J.C. Walmsley[c], B. Milkereit[d,e], R. Holmestad[a]

[a] Department of Physics, Norwegian University of Science and Technology (NTNU), Trondheim N-7491, Norway
[b] SINTEF Industry, N-7465 Trondheim, Norway
[c] Department of Materials Science and Metallurgy, University of Cambridge, CB2 3QZ, UK
[d] Chair of Materials Science, Faculty of Marine Technology and Mechanical Engineering, University of Rostock, Albert-Einstein-Str. 2, Rostock 18059, Germany
[e] Competence Centre °CALOR, Department Life, Light & Matter, Faculty of Interdisciplinary Research, University of Rostock, Albert-Einstein-Str. 25, Rostock 18059, Germany

HIGHLIGHTS

- Air cooling results in heterogenous nucleation of β-Mg_2Si and η-$MgZn_2$ on grain boundaries and dispersoids.
- Artificial ageing temperature influences the Mg-Zn (η) hardening phases orientation relationship with the aluminium matrix.
- 6xxx type hardening phases are found to coexist with the 7xxx type hardening in the T7 temper if water quenched.

GRAPHICAL ABSTRACT

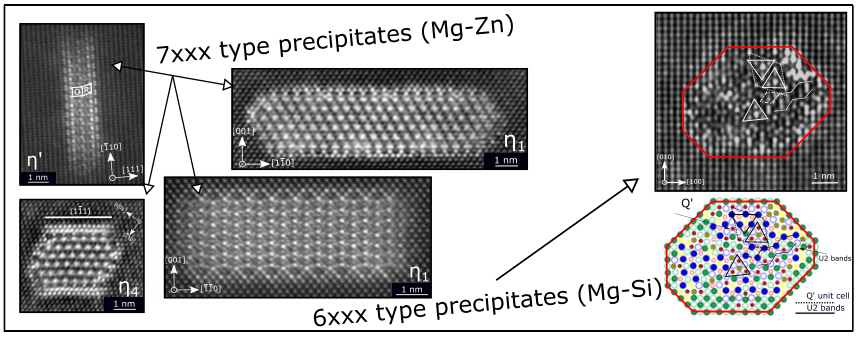

ARTICLE INFO

Article history:
Received 18 June 2019
Received in revised form 8 August 2019
Accepted 10 September 2019
Available online 24 October 2019

Keywords:
Aluminium alloys
Scanning transmission electron microscopy
Heterogeneous nucleation
Differential scanning calorimetry
η-$MgZn_2$
Precipitation

ABSTRACT

Precipitation behavior in an industrially extruded AA7003 alloy has been studied using Transmission Electron Microscopy (TEM) together with Differential Scanning Calorimetry (DSC). Air Cooling (AC) after solution heat treatment results in quench induced heterogeneous precipitation of both β-Mg_2Si and η-$MgZn_2$ phases. Detailed TEM characterisation of resulting nanoscale precipitates after AC, or Water Quenching (WQ), and subsequent artificial ageing demonstrate that η' and η_2 hardening precipitates dominate in T6, whereas the overaged T7 state contains η_2 and η_1, where the latter accounts for approximately 50% of the relative phase fraction. The T7 state in addition forms 6xxx-type hardening precipitates only after WQ. Results presented here are expected to be relevant for any Si containing 7xxx alloy and open new possibilities for development of hybrid 6xxx- and 7xxx series aluminium alloys. This is discussed with respect to potential influence on mechanical- and corrosion properties.

1. Introduction

Age hardenable Al-Zn-Mg alloys are of great importance in automotive- and aerospace applications due to their high strength to weight ratio [1-4]. High Zn/Mg ratio alloys, such as AA7003, are of particular interest due to increased extrusion speed while maintaining a yield strength of ~330 MPa [4-7]. These alloys are generally subjected to a Solution Heat Treatment (SHT) after extrusion, followed by a quench to room temperature, before Artificial Ageing (AA) at temperatures between 100 and 200 °C. Variations in mechanical processing, SHT- and AA temperatures, along with alloy composition and potential quench-induced precipitation, strongly influence

* Corresponding author.
E-mail address: adrian.lervik@ntnu.no (A. Lervik).

https://doi.org/10.1016/j.matdes.2019.108204

the resulting mechanical- and corrosion properties. Balancing these parameters has been a challenge for decades and generally one sacrifices mechanical properties to increase Stress Corrosion Cracking (SCC) resistance in 7xxx alloys, by AA to tempers other than the maximum strength yielding condition [8].

One way of measuring quench sensitivity in aluminium alloys is by Differential Scanning Calorimetry (DSC) measurement of excess specific heat capacity curves for precipitation reactions over a wide range of cooling rates [9,10]. The minimum cooling rate at which no precipitation enthalpy is detected gives the Critical Cooling Rate (CCR). All solute will thus remain in Supersaturated Solid Solution (SSSS) upon reaching room temperature, and not be precipitated on e.g. Al_3Zr dispersoids [11-16], and grain boundaries [14,15,17], which both are reported nucleation sites for the hexagonal equilibrium phase η-$MgZn_2$. DSC, in combination with Transmission Electron Microscopy (TEM), can be used to construct Continuous Cooling Precipitation (CCP) diagrams, predicting domains in which certain phases form with respect to temperature and cooling rates [18]. One example from an alloy (AA7020) with nearly similar composition to the one in the present study, revealed quench-induced precipitation of equilibrium η-$MgZn_2$ and β-Mg_2Si phases, both along grain boundaries and within the grains, by Scanning Electron Microscopy (SEM) after DSC-cooling experiments [17]. β-Mg_2Si was deduced to be the high temperature reaction occurring during slow cooling rates, disappearing when cooling >0.3 K/s. The η-$MgZn_2$ particles, observed at slightly lower temperatures disappear at cooling rates >3 K/s, thus indicating the CCR for this alloy.

In the beginning of the subsequent AA stage, coherent solute-rich Guinier-Preston (GP) zones are formed from the SSSS [19-22]. GP(I) zones, made up from Al, Mg and Zn, are fully coherent with the aluminium matrix and described as an elongated anti-phase structure with alternating arrangement of Zn and Mg rich planes [21,23,24]. GP(II) zones are described as ordering of Zn-rich layers on $\{111\}_{Al}$ with internal ordering as elongated $\langle 110\rangle_{Al}$ domains [21]. Maximum hardness is achieved by the formation of nanoscale semi-coherent metastable Mg-Zn precipitates, denoted η', while further ageing results in decreasing hardness due to coarsening, and a corresponding depletion in volume fraction of η'.

All together, there are thirteen reported orientation relationships which the nanoscale η-phase may form with the Al matrix [25-30]. The ones relevant for this study are summarised in Table 1. η' and η_2, which are plates on $\{111\}_{Al}$, were explained in detail as the Type 1 and Type 2 precipitate by Marioara et al. [30]. Type 1 consists of a rhomobohedral- (R) and an orthorombic unit (O), while Type 2 plates consist of R-units stacked pairwise or rotated 180° with respect to one another [30]. Similar stacking of R-units has been observed in the plate shaped η_1 precipitate [29,31,32]. It has recently been demonstrated that the η-precipitates may incorporate an additional flattened hexagonal sub-unit giving rise to internal stacking faults [29,31]. This sub-unit can also be described through the O- and R-units [33]. It is identical to a sub-unit found within the monoclinic Mg_4Zn_7 phase in Mg-Zn-X alloys [32,34], if the O-unit replaces its internal Zn sites with Mg. This was calculated to be as energetically favourable [30]. Incorporation of these sub-units results in a quasi-crystal like internal structure giving uncommon morphologies, making it difficult to classify their habit planes in a Bright Field (BF)-TEM image. High-Angle Annular Dark Field (HAADF) Scanning Transmission Electron Microscopy (STEM) has proven to be a more accurate method for determining the structure of these small-scale precipitate structures [29-33,35].

The general precipitation sequence may be written as:

$$SSSS \rightarrow GP(I)/GP(II) \rightarrow \eta' + \eta_{(1-13)} \rightarrow \eta(MgZn_2), \quad (1)$$

Table 1
Orientation relationships between nanoscale η-precipitates and the Al matrix demonstrated in this study. These notations are used throughout the article.

	Orientation relationship	Habit plane
η' (Type 1)	$[100]_\eta // [11\bar{2}]_{Al}$, $[120]_\eta // [\bar{1}10]_{Al}$	$(001)_\eta // (111)_{Al}$
η_2 (Type 2)	$[100]_\eta // [11\bar{2}]_{Al}$, $[120]_\eta // [\bar{1}10]_{Al}$	$(001)_\eta // (111)_{Al}$
η_1	$[100]_\eta // [1\bar{1}0]_{Al}$, $[120]_\eta // [001]_{Al}$, $(010)_\eta // (001)_{Al}$	$(001)_\eta // (110)_{Al}$
η_4	$[100]_\eta // [\bar{1}1\bar{1}]_{Al}$, $[120]_\eta // [\bar{1}12]_{Al}$, $(001)_\eta // (110)_{Al}$	$(2\bar{1}0)_\eta // (\bar{1}1\bar{1})_{Al}$

where the exact phase fraction heavily depends on the applied thermomechanical treatment. More in-depth summaries related to the nanoscale η-precipitates can be found elsewhere [29,31].

In this work, we aim for a systematic study of the microstructure in an industrially extruded AA7003. Microstructural response to variation in quench rate and AA temperature is investigated, with particular emphasis on bulk (within the grain) precipitation.

2. Material and methods

2.1. Material

The composition of the investigated AA7003 alloy, provided by Benteler Automotive Raufoss AS, is given in Table 2. The alloy was extruded into hollow rectangular profiles with dimensions 68 × 85 mm and wall thickness of 2.4 mm. The profiles were thereafter SHT at 480 °C for 30 min, followed by either a aWater Quench (WQ) or Air Cooling (AC) to room temperature. Cooling rates during AC were measured to drop from 4 to 2 K/s and 2 to 1 K/s in the temperature ranges 480–300 °C and 300–100 °C, respectively. The samples were subsequently AA at 140 °C for 17 h or 170 °C for 6 h, which are designated as the T6 and T7 tempers, respectively. Vickers hardness (HV10) values for AC-T6, AC-T7, WQ-T6 and WQ-T7 are 121, 112, 127 and 118, respectively.

2.2. Transmission electron microscopy

TEM specimens were prepared by grinding with SiC abrasive paper to ~100 μ m foil thickness, punched into 3 mm discs and thereafter electropolished with a Struers TenuPol-5 machine. An electrolyte consisting of 1/3 HNO_3 and 2/3 CH_3OH was used, and kept at temperatures between −30 and −20 °C with an applied potential of 18 V.

Precipitate crystal structures were studied in high-resolution HAADF-STEM mode using an image- and probe Cs-corrected JEOL ARM200CF operated at 200 kV, with 0.08 nm probe size, convergence semi-angle of 28 mrad and 35 mrad inner collector angle. High-resolution HAADF-STEM images were acquired using Smart Align, which involves acquiring a stack of successive low-dose images and afterwards aligning them to correct both rigid- and non-rigid scan distortions in the microcraphs [36]. Energy-Dispersive X-ray Spectroscopy (EDS) spectrum imaging was performed with an Oxford X-max 80 silicon drift detector with a detector solid angle of 0.23 sr on

Table 2
Alloy composition of the investigated alloy (in wt% and at.%) measured using optical emission spectroscopy.

	Fe	Mg	Si	Zn	Cu	Zr	Ti	Al	Zn/Mg
wt%	0.20	0.68	0.11	5.56	0.01	0.17	0.02	Bal.	8.20
at.%	0.10	0.78	0.11	2.37	0.00(4)	0.05	0.01	Bal.	3.04

a JEOL JEM-2100F operated at 200 kV in analytical STEM mode with a 1.0 nm probe size.

2.3. Differential scanning calorimetry

The precipitation behavior during cooling from solution annealing was analysed by DSC as described by Milkereit et al. [9]. Two DSC devices were used, namely a Setaram Sensys heat flux DSC for cooling rates of 0.01 to 0.1 K/s and a PerkinElmer Pyris DSC for cooling rates of 0.3 to 3 K/s. In the first device, two sample scans and one related baseline scan were measured, while in the PerkinElmer four and two sample and baseline scans were measured, respectively. The measured heat flow signal was normalised by the scanning rates and sample masses. Measured curves were averaged and the scatter plotted as introduced in Ref. [37].

3. Results

3.1. Precipitation during quenching

Fig. 1 shows excess specific heat curves for AA7003 after cooling from 480 °C with linear cooling rates from 0.01 K/s to 3 K/s. A high temperature reaction, denoted A, starts immediately at the onset of cooling in the two slowest cooling rates and is visible until ~430 °C. The peak labeled C at ~400 °C shifts towards lower temperatures and becomes increasingly suppressed with higher cooling rates. There is hint of another reaction, seen as a shoulder on its high temperature side labeled B. B & C are visible in all cooling conditions up to 1 K/s and may still be present at the highest cooling rate of 3 K/s.

At least two overlapping peaks (D & E) are observed in the region 315–150 °C. These also become suppressed at higher cooling rates and seem to nearly disappear already at 1 K/s. The peaks shift towards higher temperatures with increasing cooling rates and, consequently, overlap with the previously mentioned high temperature peaks. A low temperature peak, F, is observed at <100 ° C.

TEM observations of AC cooled samples before AA reveal quench induced precipitates, of both η-$MgZn_2$ and β-Mg_2Si, nucleating heterogeneously on grain boundaries, Al_3Zr dispersoids and Al-Fe-Si particles. Representative BS-STEM micrographs are shown in Fig. 2. Fig. 2A and B shows precipitation on two grain boundaries. In Fig. 2A, there are two β-Mg_2Si particles present together with Al_3Zr dispersoids, while in Fig. 2 B there is a fine population of small η-$MgZn_2$ precipitates. Fig. 2 C and D shows typical observations made in the bulk where Fig. 2C shows nucleation of β-Mg_2Si on an Al-Fe-Si particle and Fig. 2D shows a complex nucleation cluster, where Al_3Zr, β-Mg_2Si, η-$MgZn_2$ and dislocations are present. It is not clear which are the nucleation sites for each phase in Fig. 2 D. Notice the low contrast from the β-Mg_2Si particle. The chemical compositions of the phases present were verified using EDS (not shown). No evidence of homogeneous nucleation of hardening phases was observed during AC.

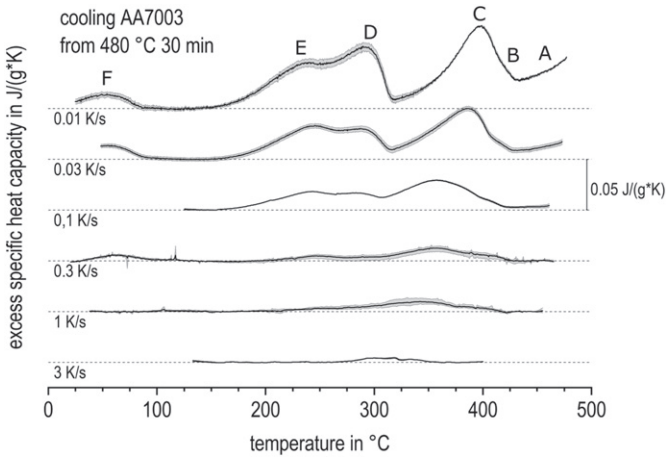

Fig. 1. DSC cooling curves for AA7003 with varying cooling rates from 0.01 to 3 K/s. The alloy was subjected to a solution heat treatment at 480 °C for 30 min prior to cooling.

3.2. Microstructure in aged tempers

Similar to the AC-T4 temper, the final AC-T6/T7 tempers have significant amounts of heterogeneous nucleated precipitates. Fig. 3 shows an example of a typical bulk microstructure acquired by HAADF-STEM. Multiple heterogeneous nucleation sites amid the bulk hardening phases are observed. Precipitate Free Zones (PFZ) are found to form around these nucleation sites. In Fig. 3, taken in the AC-T6 temper, both β-Mg_2Si and η-$MgZn_2$ are found together with two Al_3Zr particles. It is not clear whether Al_3Zr is the primary nucleation site, or if η-$MgZn_2$ can serve as a nucleation site for β-Mg_2Si, or vice versa. Another example, from the overaged AC-T7 condition, is shown in Fig. 4, where three η-particles and one β-Mg_2Si are nucleated onto a Al-Fe-Si particle. In both Figs. 3 and 4, the β-Mg_2Si particles are not distinguishable solely from the HAADF- and BF-STEM micrographs. This emphasises the difficulty of observing this phase in this system, unless it is explicitly searched for.

Bulk microstructures in T6 and T7 after WQ appear similar to the AC and aged tempers, as in Fig. 3, apart from the heterogeneous nucleation. No observations of β-Mg_2Si were made on the typical nucleation sites demonstrated in Fig. 2. However, η-$MgZn_2$ particles were occasionally observed on Al_3Zr and Al-Fe-Si dispersoids. It is possible that these have formed during AA as they were not observed in the as-WQ samples. On grain boundaries, η-$MgZn_2$ particles were observed in a similar manner as for the AC tempers.

Only the η-precipitates described in Table 1 were observed in the present work. BF-TEM micrographs along $[110]_{Al}$ are shown for all four final tempers in Fig. 5. In this projection, 2/4, 1/3 and 1/6 of the precipitates with habit planes $\{111\}_{Al}$, $\{100\}_{Al}$ and $\{110\}_{Al}$, respectively, are observed edge on. The remaining precipitates are projections of equivalent precipitates on similar family planes, undefined faulted phases and in some rare cases the cross-section of η_4. In order to obtain a relative fraction of phases present, the number of precipitates with habit planes $\{111\}_{Al}$, $\{100\}_{Al}$ and $\{110\}_{Al}$ were counted and multiplied by 2, 3 and 6, respectively. This means only counting the edge-on precipitates and multiplying in order to account for the identical precipitates lying on equivalent planes not observed in the zone axis. As summarised in Table 3, both the T6 tempers are dominated by η' and η_2, while the T7 tempers are dominated by η_1 and η_2. Due to uncertainties when measuring the dimensions of particles from BF-TEM images, such as in Fig. 5, an upper threshold for the minor dimension (thickness) of measured particles with $\{111\}_{Al}$ habit plane was set to 20 Å, slightly higher than its distinct thickness of $7\times\{111\}_{Al}$ (≈16.4 Å) as shown in Fig. 6A [30], in order to separate η' from η_2. It is then observed that in both T7 states, η' is non-existent. Several authors have suggested the reaction $\eta' \rightarrow \eta_2$ as a possible transformation [26,38-40]. Furthermore, from Table 3 and Fig. 5 it is clear that both dimensions of the precipitates are larger when aged at 170 °C.

The phase with habit plane $\{110\}_{Al}$, marked with question marks in Fig. 5B and D, was not observed by high-resolution HAADF-STEM when imaging along $[110]_{Al}$ or $[100]_{Al}$ axis. It is likely to be another orientation relation which η may form with aluminium or a faulted structure growing along the $[100]_{Al}$ direction.

η' hardening precipitates with structures similar to those reported before were observed in all conditions. An example is

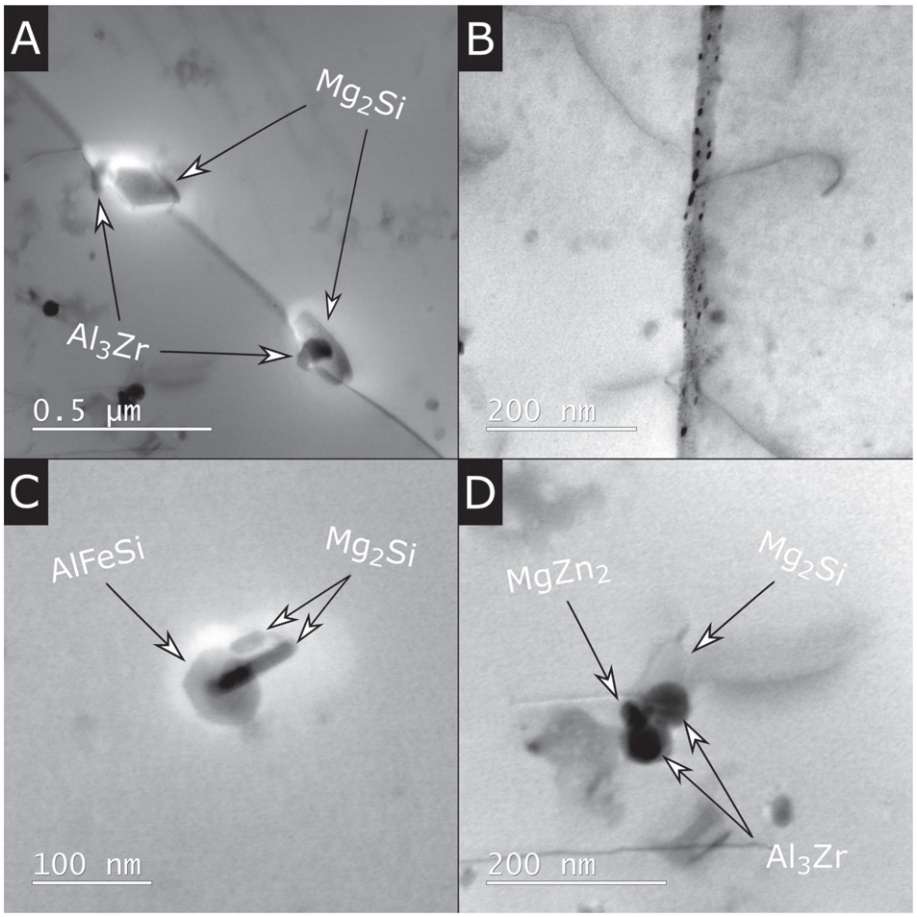

Fig. 2. BF-STEM micrographs from the AC-T4 condition, showing typical heterogeneous nucleation sites. A) Two β-Mg_2Si phases on a grain boundary, with an Al_3Zr particle in the nucleation site. B) A grain boundary with fine population of small η-$MgZn_2$ precipitates. C) Two β-Mg_2Si particles nucleated on a Al-Fe-Si particle. D) A nucleation site including Al_3Zr dispersoids, η-$MgZn_2$, β-Mg_2Si and dislocation lines. Notice the low contrast from the β-Mg_2Si phase. The chemical composition of the phases in all micrographs has been verified using EDS.

shown in Fig. 6A, and is the η' (Type 1) precipitate [30]. This precipitate can also incorporate defects, such as a roto-inversion center, shown in Fig. 6B. η_2 (Type 2) is also frequently observed, although not shown here.

η_1 was observed along the two axis: $[001]_\eta//[110]_{Al}$ and $[100]_\eta//[1\bar{1}0]_{Al}$, shown in Fig. 6C and D, respectively. Fig. 6C and D shows the habit interface created by the $(010)_\eta$ plane aligned with the $(001)_{Al}$ plane, rotated 90° across $[001]_{Al}$. This phase is a plate shaped precipitate with habit plane $(010)_\eta//(001)_{Al}$.

Furthermore, cross-sections with orientation relationship corresponding to those reported for η_4 [26], were observed in the T7 tempers, and one is shown in Fig. 6E. It has been proposed as a rod/lath with habit planes on $\{111\}_{Al}$ with the following orientation relationship: $(2\bar{1}0)_\eta//(\bar{1}1\bar{1})_{Al}$ and $[001]_\eta//[110]_{Al}$, which is in agreement with the presented micrograph. Two $\{111\}_{Al}$ planes enriched with high Z elements (Zn or Cu) are observed on both sides of the precipitate.

A range of faulted structures were observed in the present work, and one is shown Fig. 6F. Orientation relationships for these precipitates cannot be simply defined. They do however stack the same R-unit, but do addition incorporate the flattened hexagonal sub-units indicated as the white hexagon, separating regions of well ordered structures. In the given example, there is a previously unreported semi-coherent interface present along the $[1\bar{1}\bar{4}]_{Al}$ direction, which connects to the unfaulted structure marked in the figure. The orientation can thus be written as $[100]_\eta//[110]_{Al}$ and $(010)_\eta//(2\bar{2}1)_{Al}$. This has never been observed for a free-standing non-faulted precipitate. Similar faulted structures have been observed within the η_1 and η_2 precipitates [29,31-33].

3.3. Observation of 6xxx hardening phases

As no Mg_2Si-phases were observed in the T6 and T7 tempers at the typical heterogeneous nucleation sites after WQ, this would suggest that Si still remains in solid solution. However, STEM-EDS of WQ-T7 revealed a fine population of small Mg-Si precipitates between the slightly larger η precipitates. This is shown in Fig. 7, where EDS spectrum images are obtained across a grain boundary. The Si signal correlates with some Mg sites, but not with Zn. They do however appear close to each other, since the Mg-Si particles are observed to occasionally nucleate on the η-particles, or vice-versa, as demonstrated by HAADF-STEM in Fig. 7.

High-resolution observations along $[100]_{Al}$ reveal Mg-Si phases with disordered crystal structures, similar to what has been observed in the 6xxx aluminium system [41,42]. These are small needles, distributed homogeneously within a grain. The cross-section of one example is shown in Fig. 8. It consists of Q' and U2 building blocks connected by a near hexagonal Si network [43], demonstrated by the overlaid atomic positions in Fig. 8. Furthermore, there are indications of either Zn or Cu enrichment at the interface which gives localised bright atomic columns. Based on the atomic overlay the composition

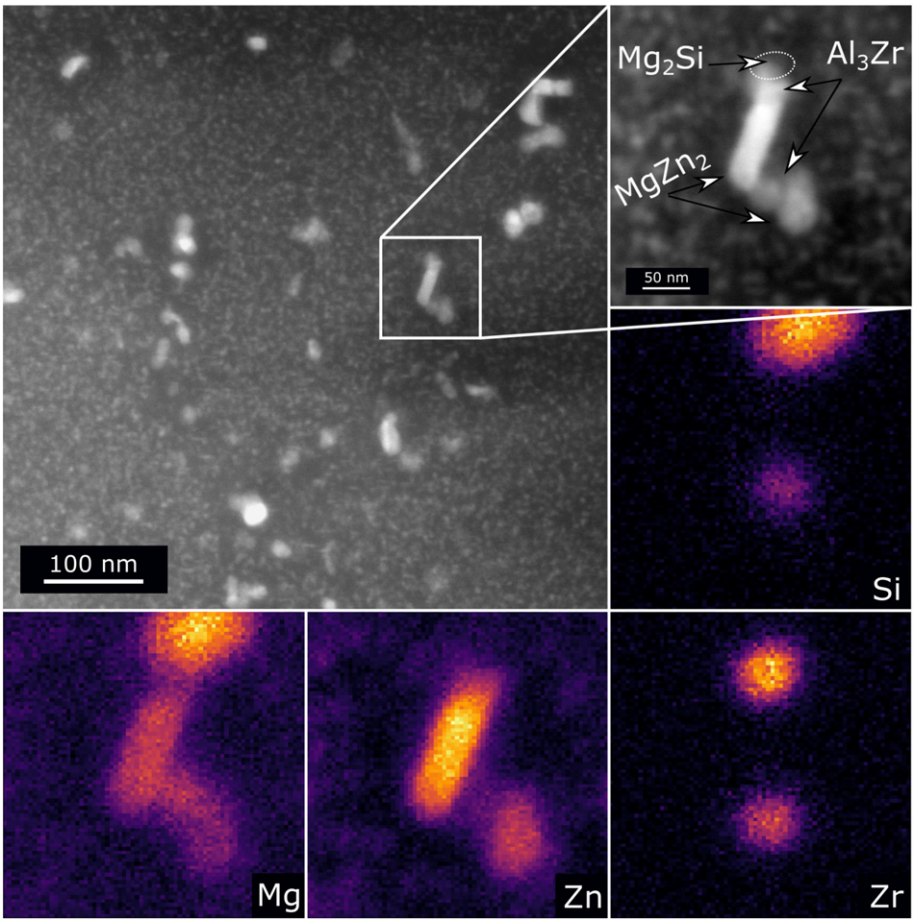

Fig. 3. HAADF-STEM micrograph showing heterogeneous nucleation in the bulk microstructure of the AC-T6 temper. The corresponding EDS spectrum images for Mg, Si, Zn and Zr from the indicated area are shown. β-Mg_2Si, η-$MgZn_2$ and Al_3Zr are observed in the particle agglomerate.

of the precipitate in Fig. 8 results in $Al_{0.27}(Cu,Zn)_{0.17}Mg_{0.29}Si_{0.27}$ giving a Mg/Si ratio close to 1 which is typical for 6xxx type hardening phases [33,44].

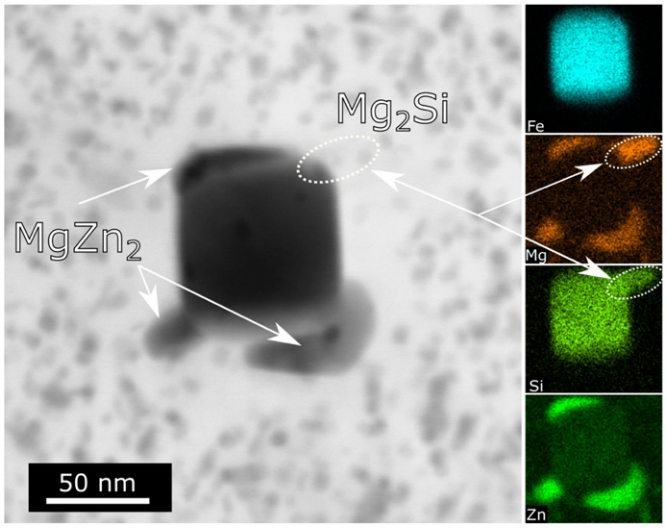

Fig. 4. STEM-BF micrograph of a Al-Fe-Si particle in the AC-T7 condition. Three η-$MgZn_2$ precipitates can clearly be observed in the micrograph and the corresponding EDS map. A smaller β-Mg_2Si particle is also nucleated on the particle, but cannot be seen in the STEM image. As indicated, this is only revealed in the corresponding Mg and Si EDS spectrum images.

4. Discussion

During AC from solution annealing, there are multiple heterogeneous precipitation reactions occurring. Observed nucleation sites are grain boundaries in addition to Al_3Zr and Al-Fe-Si dispersoids. Both η-$MgZn_2$ and β-Mg_2Si were found on these sites, as demonstrated in Fig. 2. These precipitation events must be related to the observed peaks in the DSC cooling curves in Fig. 1, where at least 6 precipitation reactions are occurring.

A complete understanding of the peaks denoted A–F in Fig. 1, would require extensive TEM investigations following interrupted quenching. However, a qualitative discussion is possible based on previous work. The origin of peak A, directly visible at the onset of cooling in the two slowest cooling rates, is unclear. It may be related to the formation of Al-Fe-Si dispersoids or β-Mg_2Si. Kemsies et al. demonstrated that the previously described "stable" Al-Fe-Mn-Si dispersoids can partially dissolve at temperatures above ~450 °C, giving a substantial signal in the DSC curves [37]. As the reaction is diffusion driven, it may become suppressed with higher cooling rates, which is similar to what is observed in present work.

Two peaks, B & C, are observed in the region 430–320 °C, with B appearing as a shoulder on the high temperature side in the range 430–400 °C. These may correspond to β-Mg_2Si, which is suggested to occur in this temperature region in AA7020 [17]. The formation enthalpies of β-Mg_2Si and η-$MgZn_2$ are about one order of magnitude apart [10,45]. This might suggest that β-Mg_2Si can appear significant in the DSC cooling curves, although it is lower in volume fraction. In the region 350–170 °C, there are two peaks, D & E, where

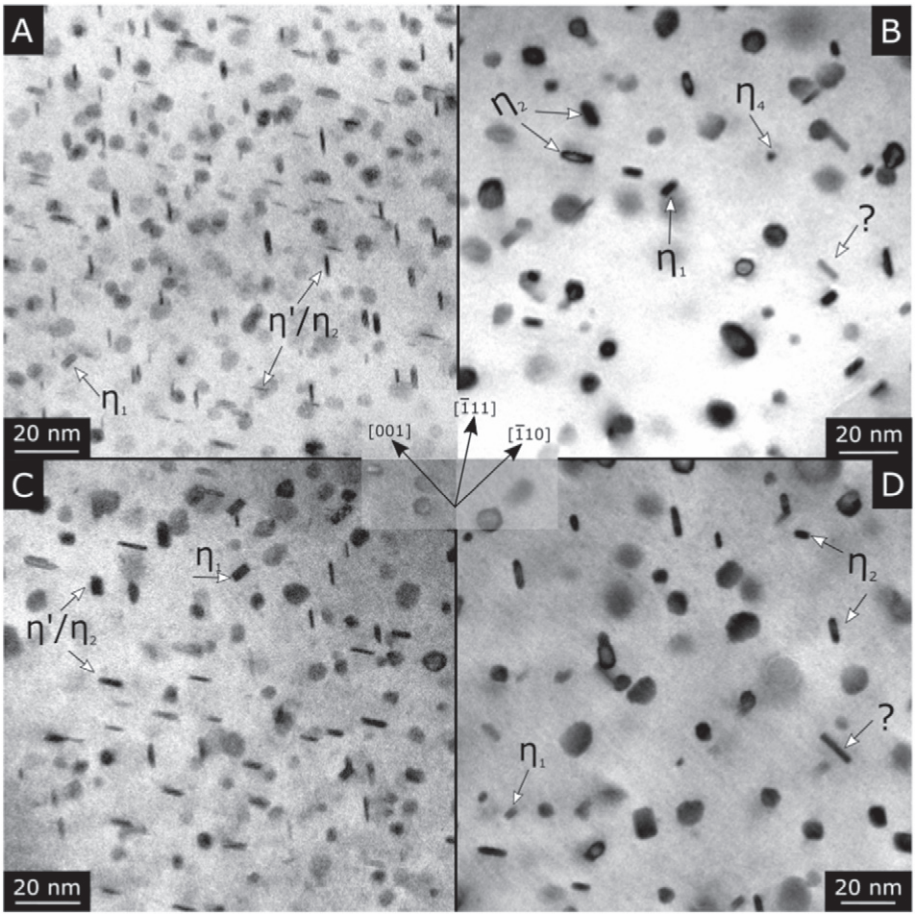

Fig. 5. BF-TEM micrographs of bulk precipitates oriented along the $[110]_{Al}$ direction with the same indicated coordinate system. (A) AC sample in T6 and T7 (B). (C) WQ sample in T6 and T7 (D). The precipitates are generally larger in the T7 conditions which contains ~50% η_1 precipitates growing on the $\{100\}_{Al}$ planes, in addition to η'/η_2 on $\{111\}_{Al}$. '?' with habit plane $\{110\}_{Al}$ has not been identified.

at least one should correspond to η-$MgZn_2$, as has been reported to precipitate within a very similar temperature range in other Al-Zn-Mg alloys [15,10,17,46]. The reason for the two peaks in this region is unclear. The final peak observed at $<100^\circ$ C most likely corresponds to homogeneous distribution of cluster nucleation [47].

As discussed, there are more peaks in the DSC cooling curves than observed phases. One possible explanation for this is the undetected presence of other phases such as T-$Al_2Mg_3Zn_3$. Another explanation could be that the same phase may yield different peaks in the DSC curves owing to different nucleation sites and/or morphology. In binary Al-Si, it was demonstrated that the same Si-phase resulted in two observable peaks in the DSC curves due to different aspect ratios [48]. Similar observations were made for Mg_2Si in a ternary Al-Mg-Si alloy [49].

It is evident from the DSC curves that precipitation may occur if the cooling rate is insufficient to suppress all the reaction events occurring. In this alloy it is made clear by TEM, and supported by DSC, that the material is quench sensitive during AC. From Fig. 1, precipitation enthalpy is still detected at the highest measured cooling rate of 3 K/s, indicating that the CCR for our alloy is higher than this.

With regard to the nanoscale η-phases it seems that the artificial ageing temperature is the controlling parameter for both precipitate orientation and size. The hardness in the T7 tempers is 9 (HV10) less than for their T6 counterparts due to coarser precipitates. The two prior cooling conditions seem to have minimal influence on bulk precipitate size and orientation, although some solute is consumed in heterogeneous precipitation during AC reducing the hardness by 6 (HV10) when comparing the AC and WQ tempers. As shown in Fig. 6, there are many orientations which the nanoscale η precipitates can form with respect to the aluminium matrix. Introducing exact 3D models for η_1 and η_4 is outside the scope of present work, but should be conducted in future and calculated using Density Functional Theory (DFT) calculations in a similar manner as for η' and η_2 [30].

A homogeneous distribution of 6xxx hardening phases were only observed in the WQ-T7 state. Extensive STEM work was carried out to determine if these phases were present in WQ-T6 (ageing at 140 °C), but none were observed. This could indicate that these phases only form when ageing at relatively high temperatures with respect to what is typical in 7xxx alloys. In alloys subjected to Retrogression and Reageing (RRA), this may be important when performing the retrogression stage at elevated temperatures if the alloy contains Si. More work needs to be done in order to understand the kinetics of the observed concurrent precipitation and its influence on hardness. Comparing hardening kinetics in a similar alloy like the present but with 0.0 wt.% Si is a possible approach.

To the authors knowledge, there is only one report on precipitation of nanoscale 6xxx type hardening phases in 7xxx alloys. Hansen et al. studied Cu-free high Zn/Mg ratio 7xxx alloys with varying Si amounts and compared microstructures after SHT at 450 and 550 °C [50]. The higher SHT temperature dissolved primary Mg_2Si-phases resulting

Table 3
Relative fraction of identifiable plate shaped η hardening phases. The average minor dimension (thickness) and major dimension (diameter) and corresponding standard deviation are given as sorted based on the precipitate orientation. In addition, the upper and lower value within the measured population for the two dimensions is given.

	AC								WQ							
	T6				T7				T6				T7			
	η'	η_2	η_1	?	η'	η_2	η_1	?	η'	η_2	η_1	?	η'	η_2	η_1	?
Measurements (#)	62	22	2	0	0	55	46	8	24	29	5	0	1	47	29	8
Relative fraction (%)	71	25	4	0	0	37	47	16	40	48	12	0	0	41	38	21
Avg. thickness (nm)	1.40 ± 0.21	2.25 ± 0.43	–	–	–	3.55 ± 0.86	3.87 ± 1.48	3.73 ± 1.93	1.59 ± 0.21	2.49 ± 0.45	3.33 ± 0.39	–	–	3.33 ± 0.80	3.84 ± 1.18	2.89 ± 1.18
Upper/lower thickness (nm)	1.88/1.04	3.34/2.01	–	–	–	6.67/1.95	9.06/1.77	8.79/2.50	1.98/1.04	4.06/2.07	3.82/2.68	–	–	6.49/2.45	6.30/2.32	3.82/2.12
Avg. diameter (nm)	5.42 ± 1.19	6.08 ± 1.19	–	–	–	8.84 ± 2.23	7.27 ± 1.96	10.25 ± 3.04	6.16 ± 1.38	6.44 ± 1.29	4.92 ± 0.78	–	–	8.13 ± 2.00	7.41 ± 1.77	10.24 ± 2.20
Upper/lower diameter (nm)	8.32/2.58	8.67/4.38	–	–	–	13.73/4.82	12.10/4.21	15.59/6.14	9.51/3.56	9.08/3.68	6.30/3.95	–	–	13.72/4.58	11.05/3.39	14.39/7.12

Fig. 6. HAADF-STEM micrographs of η type precipitates in the WQ samples. A–B: η' (Type 1) precipitate along $[11\bar{2}]_{Al}$, showing a defect free (A) and a faulted variant (B). C–D: η_1 along $[001]_\eta//[110]_{Al}$ and $[010]_\eta//[\bar{1}10]_{Al}$ in (C) and (D), respectively. (E) is a micrograph of the cross-section of η_4 with the interface relation as $(2\bar{1}0)_\eta//(\bar{1}1\bar{1})_{Al}$. (F) Shows a highly disordered η precipitate. Notice the similar R- and O-units as in η', in addition to the flattened hexagon which can be described in two ways. A and B are obtained in WQ–T6, while the rest are from WQ–T7.

in precipitation of Mg-Si hardening phases during the subsequent AA, contributing to the overall hardness.

There are, on the other hand, reports on the effect of adding Zn to 6xxx alloys. Saito et al. demonstrated that Zn can be incorporated into 6xxx hardening phases without disrupting the underlying Si-network [51]. Partial substitution both on and between Si-network columns was observed, as well as a tendency for Zn to segregate at particle/matrix interfaces. No η-phases were observed in the bulk microstructure, even with up to 1 wt.% Zn addition. By adding up to

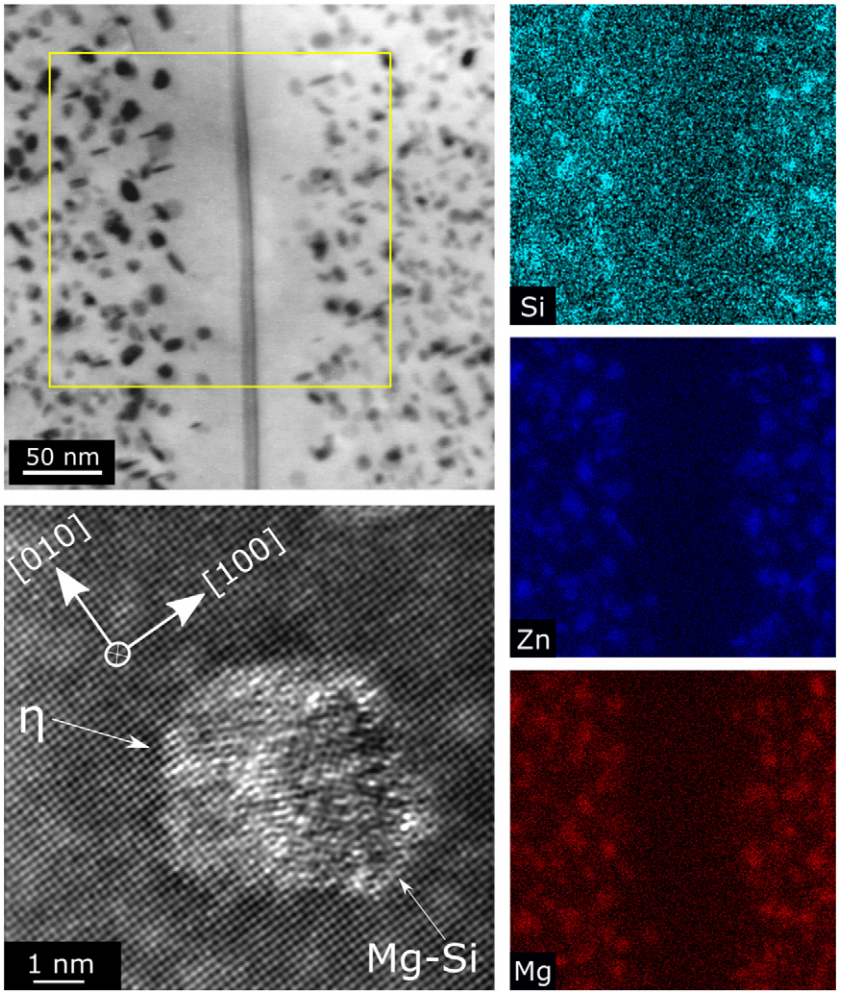

Fig. 7. BF-STEM image of a grain boundary in WQ-T7. The yellow square indicate where the corresponding Si, Zn and Mg EDS spectrum images are obtained. There are small regions in which Mg correlates with Si, but not with Zn. The Si and Zn signal may overlap since the 6xxx type hardening precipitate often are observed together with an η-type precipitate as shown by the high-resolution HAADF-STEM micrograph taken along $[100]_{Al}$.

3 wt.% Zn in an Al-Mg-Si alloy, Ding et al. were able to precipitate η in the bulk microstructure [52].

With respect to material properties, Gong et al. reported improvements in fatigue strength with increasing Si content in a 7xxx alloy [53]. She et al. reported a decrease in SCC susceptibility and decrease in tensile strength with increasing Si content [54]. The role of 6xxx precipitates on such properties could be explored further by optimising composition and thermal treatments. In relation to SCC, authors have claimed hardening phases (or their interfaces), as well as β-Mg_2Si, as important hydrogen trapping sites [55-58]. Modelling of these properties requires accurate knowledge of the precipitates present in the microstructure. However, it is unclear how the η-phase(s), β-Mg_2Si and 6xxx hardening phases compare with respect to hydrogen trapping energies and this should be explored further. Understanding hydrogen partition within the microstructure may suggest ways to reduce hydrogen concentration at grain boundaries and alleviate SCC susceptibility.

Optimising thermomechanical treatments could make use of the excess Si commonly found in 7xxx alloys by ensuring complete dissolution of the β-Mg_2Si with respect to the SHT and limiting quench induced precipitation. This may open possibilities for development of new hybrid 6xxx/7xxx series aluminium alloys.

5. Conclusion

An industrially extruded AA7003 alloy is investigated after different thermal treatments following either air cooling or water quenching from solution heat treatment. The main findings are:

1. Air cooling results in heterogeneous nucleation of β-Mg_2Si and η-$MgZn_2$ particles on grain boundaries and dispersoids.
2. The critical cooling rate for this alloy is higher than 3 K/s.
3. Bulk microstructures are dominated by η' & η_2 and η_1 & η_2 hardening precipitates after artificially ageing at 140 and 170 °C, respectively. This is independent of the prior water- or air cooling.
4. In the WQ-T7 state, 6xxx-type hardening precipitates coexist with the 7xxx hardening precipitates.

The results presented provide important fundamental insight into bulk microstructures, which are important for optimisation of thermomechanical treatments in 7xxx alloys containing Si.

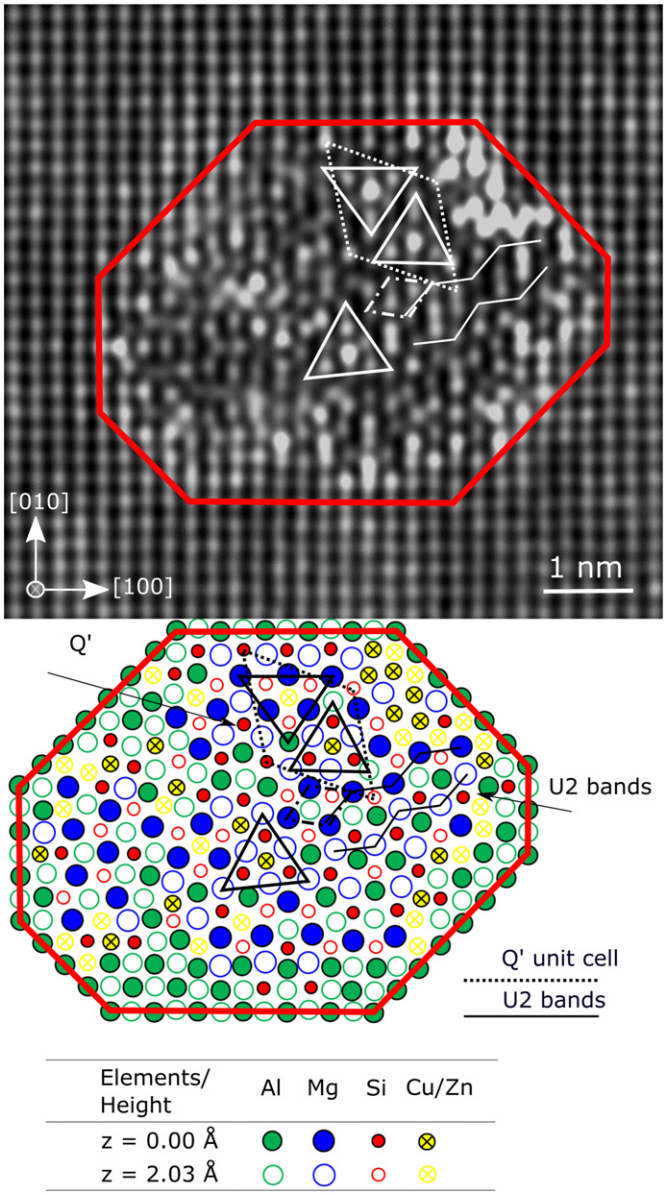

Fig. 8. HAADF-STEM micrograph of a disordered 6xxx type precipitate (top) and suggested atomic overlay (bottom). The micrograph has been fast Fourier transformed with a circular mask removing periods shorter than 0.15 nm. The micrograph is obtained in the WQ–T7 condition along the $[100]_{Al}$ direction.

CRediT authorship contribution statement

A. Lervik: Conceptualization, Data curation, Formal Analysis, Investigation, Writing - original draft. **C.D. Marioara:** Formal Analysis, Investigation, Writing - review & editing. **M. Kadanik:** Data Curation, Investigation. **J.C. Walmsley:** Funding acquisition, Supervision, Writing - review & editing. **B. Milkereit:** Formal analysis, Investigation, Supervision, Writing - review & editing. **R. Holmestad:** Funding acquisition, Supervision, Writing - review & editing.

Acknowledgments

L. Lodgaard and Benteler Automotive Raufoss AS is greatly acknowledged for providing the material and being involved in the discussions. This work was supported by the KPN project "FICAL" (Research Council of Norway (NFR):247598), co-financed by The Research Council of Norway (NFR), and the industrial partners Hydro, Gränges, Benteler Automotive Raufoss AS and Steertec Raufoss. The (S)TEM work was conducted on the NORTEM (Research Council of Norway (NFR):197405) infrastructure at the TEM Gemini Centre, Trondheim, Norway.

References

[1] G. Totten, D. MacKenzie, Handbook of Aluminum, Marcel Dekker, New York, 2003.
[2] T. Shikama, S. Yoshihara, Highly SCC resistant 7000-series aluminum alloy extrusion, KOBELCO Technol. Rev. (2017) 65–68. http://www.kobelco.co.jp/english/ktr/pdf/ktr_35/065-068.pdf.
[3] T. Dursun, C. Soutis, Recent developments in advanced aircraft aluminium alloys, Mater. Des. 56 (2014) 862–871. https://doi.org/10.1016/j.matdes.2013.12.002.
[4] A. Reyes, O.S. Hopperstad, O.G. Lademo, M. Langseth, Modeling of textured aluminum alloys used in a bumper system: material tests and characterization, Comput. Mater. Sci. 37 (2006) 246–268. https://doi.org/10.1016/j.commatsci.2005.07.001.
[5] O. Jensrud, High Strength Aluminium Alloys Extrusions — A Review of the Thermo-Mechanical-Process in High Performance Profile Manufacturing, Progress in Extrusion Technology and Simulation of Light Metal Alloys, Key Engineering Materials, 491, Trans Tech Publications. 2012, pp. 11–18. https://doi.org/10.4028/www.scientific.net/KEM.491.11.
[6] M.C. Paulisch, N. Wanderka, M. Haupt, S. Selve, I. Driehorst, W. Reimers, The influence of heat treatments on the microstructure and the mechanical properties in commercial 7020 alloys, Mater. Sci. Eng. A 626 (2015) 254–262. https://doi.org/10.1016/j.msea.2014.12.040.
[7] M.C. Paulisch, M. Lentz, H. Wemme, A. Andrich, I. Driehorst, W. Reimers, The different dependencies of the mechanical properties and microstructures on hot extrusion and artificial aging processing in case of the alloys Al 7108 and Al 7175, J. Mater. Process. Technol. 233 (2016) 68–78. https://doi.org/10.1016/j.jmatprotec.2016.02.012.
[8] A.C.U. Rao, V. Vasu, M. Govindaraju, K.V.S. Srinadh, Stress corrosion cracking behaviour of 7xxx aluminum alloys: a literature review, Trans. Nonferrous Metals Soc. China (English Edition) 26 (2016) 1447–1471. https://doi.org/10.1016/S1003-6326(16)64220-6.
[9] B. Milkereit, O. Kessler, C. Schick, Recording of continuous cooling precipitation diagrams of aluminium alloys, Thermochim. Acta 492 (2009) 73–78. https://doi.org/10.1016/j.tca.2009.01.027.
[10] M.J. Starink, B. Milkereit, Y. Zhang, P.A. Rometsch, Predicting the quench sensitivity of Al-Zn-Mg-Cu alloys: a model for linear cooling and strengthening, Mater. Des. 88 (2015) 958–971. https://doi.org/10.1016/j.matdes.2015.09.058.
[11] M. Conserva, E. Di Russo, O. Caloni, Comparison of the influence of chromium and zirconium on the quench sensitivity of Al-Zn-Mg-Cu alloys, Metall. Trans. 2 (1971) 1227–1232. https://doi.org/10.1007/BF02664256.
[12] A. Deschamps, Y. Bréchet, Influence of quench and heating rates on the ageing response of an Al-Zn-Mg-(Zr) alloy, Mater. Sci. Eng. A 251 (1998) 200–207. https://doi.org/10.1016/S0921-5093(98)00615-7.
[13] A. Deschamps, Y. Bréchet, Nature and distribution of quench-induced precipitation in an Al-Zn-Mg-Cu alloy, Scr. Mater. 39 (1998) 1517–1522. https://doi.org/10.1016/S1359-6462(98)00357-1.
[14] D. Godard, P. Archambault, E. Aeby-Gautier, G. Lapasset, Precipitation sequences during quenching of the AA 7010 alloy, Acta Mater. 50 (2002) 2319–2329. https://doi.org/10.1016/S1359-6454(02)00063-0.
[15] A. Deschamps, G. Texier, S. Ringeval, L. Delfaut-Durut, Influence of cooling rate on the precipitation microstructure in a medium strength Al-Zn-Mg alloy, Mater. Sci. Eng. A 501 (2009) 133–139. https://doi.org/10.1016/j.msea.2008.09.067.
[16] Y. Zhang, C. Bettles, P.A. Rometsch, Effect of recrystallisation on Al3Zr dispersoid behaviour in thick plates of aluminium alloy AA7150, J. Mater. Sci. 49 (2014) 1709–1715. https://doi.org/10.1007/s10853-013-7856-x.
[17] Y. Zhang, B. Milkereit, O. Kessler, C. Schick, P.A. Rometsch, Development of continuous cooling precipitation diagrams for aluminium alloys AA7150 and AA7020, J. Alloys Compd. 584 (2014) 581–589. https://doi.org/10.1016/j.jallcom.2013.09.014.
[18] B. Milkereit, N. Wanderka, C. Schick, O. Kessler, Continuous cooling precipitation diagrams of Al-Mg-Si alloys, Mater. Sci. Eng. A 550 (2012) 87–96. https://doi.org/10.1016/j.msea.2012.04.033.
[19] H. Inoue, T. Sato, Y. Kojima, T. Takahashi, The temperature limit for GP zone formation in an Al-Zn-Mg alloy, Metall. Mater. Trans. A 12 (1981) 1429–1434. https://doi.org/10.1007/BF02643687.
[20] X.J. Jiang, B. Noble, B. Holme, G. Waterloo, J. Taftø, Differential scanning calorimetry and electron diffraction investigation on low-temperature aging in Al-Zn-Mg alloys, Metall. Mater. Trans. A 31 (2000) 339–348. https://doi.org/10.1007/s11661-000-0269-x.
[21] L.K. Berg, J. Gjønnes, V. Hansen, X.Z. Li, M. Knutson-Wedel, G. Waterloo, D. Schryvers, L.R. Wallenberg, GP-zones in Al-Zn-Mg alloys and their role in artificial aging, Acta Mater. 4 (2001) 3443–3451. https://doi.org/10.1016/S1359-6454(01)00251-8.
[22] G. Sha, A. Cerezo, Early-stage precipitation in Al-Zn-Mg-Cu alloy (7050), Acta Mater. 52 (2004) 4503–4516. https://doi.org/10.1016/j.actamat.2004.06.025.

[23] C. Wolverton, Crystal structure and stability of complex precipitate phases in Al-Cu-Mg-(Si) and Al-Zn-Mg alloys, Acta Mater. 49 (2001) 3129–3142. https://doi.org/10.1016/S1359-6454(01)00229-4.

[24] K. Matsuda, A. Kawai, K. Watanabe, S. Lee, C.D. Marioara, S. Wenner, K. Nishimura, T. Matsuzaki, N. Nunomura, T. Sato, R. Holmestad, S. Ikeno, Extra electron diffraction spots caused by fine precipitates formed at the early stage of aging in Al-Mg-X (X = Si, Ge, Zn)-Cu alloys, J. Jpn. Inst. Light Met. 58 (2017) 167–175. https://doi.org/10.2464/jilm.67.186.

[25] P. Thackary, The nature and morphology of precipite in Al-Zn-Mg alloys, J. Inst. Met. 96 (1968) 7.

[26] J. Gjønnes, C.J. Simensen, An electron microscope investigation of the microstructure in an aluminium-zinc-magnesium alloy, Acta Metall. 18 (1970) 881–890. https://doi.org/10.1016/0001-6160(70)90016-7.

[27] H.P. Degischer, W. Lacom, A. Zahra, Y.C. Zahra, Decomposition processes in an Al-5% Zn-1% Mg alloy — part II: electron microscopic investigations, Zeitschrift Z. Metallkd. 71 (1980) 213–238.

[28] H. Löffler, I. Kovács, J. Lendvai, Review decomposition processes in Al-Zn-Mg alloys, J. Mater. Sci. 18 (1983) 2215–2240. https://doi.org/10.1007/BF00541825.

[29] T.-F. Chung, Y.-L. Yang, M. Shiojiri, C.-N. Hsiao, W.-C. Li, C.-S. Tsao, Z. Shi, J. Lin, J.-R. Yang, An atomic scale structural investigation of nanometre-sized η precipitates in the 7050 aluminium alloy, Acta Mater. (2019) https://doi.org/10.1016/j.actamat.2019.05.041.

[30] C.D. Marioara, W. Lefebvre, S.J. Andersen, J. Friis, Atomic structure of hardening precipitates in an Al-Mg-Zn-Cu alloy determined by HAADF-STEM and first-principles calculations: relation to η-MgZn2, J. Mater. Sci. 48 (2013) 3638–3651. https://doi.org/10.1007/s10853-013-7158-3.

[31] A. Bendo, K. Matsuda, S. Lee, K. Nishimura, N. Nunomura, H. Toda, M. Yamaguchi, T. Tsuru, K. Hirayama, K. Shimizu, H. Gao, K. Ebihara, M. Itakura, T. Yoshida, S. Murakami, Atomic scale HAADF-STEM study of η and η_1 phases in peak-aged Al-Zn-Mg alloys, J. Mater. Sci. 53 (2018) 4598–4611. https://doi.org/10.1007/s10853-017-1873-0.

[32] A. Bendo, T. Maeda, K. Matsuda, A. Lervik, R. Holmestad, C.D. Marioara, K. Nishimura, N. Nunomura, H. Toda, M. Yamaguchi, K.-i. Ikeda, T. Homma, Characterisation of structural similarities of precipitates in Mg-Zn and Al-Zn-Mg alloys systems, Philos. Mag. 0 (2019) 1–17. https://doi.org/10.1080/14786435.2019.1637032.

[33] S.J. Andersen, C.D. Marioara, J. Friis, S. Wenner, R. Holmestad, Precipitates in aluminium alloys, Adv. Phys. X 3 (2018) 790–813. https://doi.org/10.1080/23746149.2018.1479984.

[34] A. Singh, J. Rosalie, Lattice correspondence and growth structures of monoclinic Mg4Zn7 phase growing on an icosahedral quasicrystal, Crystals 8 (2018) 194. https://doi.org/10.3390/cryst8050194.

[35] Y.Y. Li, L. Kovarik, P.J. Phillips, Y.F. Hsu, W.H. Wang, M.J. Mills, High-resolution characterization of the precipitation behavior of an Al-Zn-Mg-Cu alloy, Philos. Mag. Lett. 92 (2012) 166–178. https://doi.org/10.1080/09500839.2011.652682.

[36] L. Jones, H. Yang, T.J. Pennycook, M.S.J. Marshall, S. Van Aert, N.D. Browning, M.R. Castell, P.D. Nellist, Smart Align — a new tool for robust non-rigid registration of scanning microscope data, Adv. Struct. Chem. Imaging 1 (2015) 8. https://doi.org/10.1186/s40679-015-0008-4.

[37] R.H. Kemsies, B. Milkereit, S. Wenner, R. Holmestad, O. Kessler, In situ DSC investigation into the kinetics and microstructure of dispersoid formation in Al-Mn-Fe-Si(-Mg) alloys, Mater. Des. 146 (2018) 96–107. https://doi.org/10.1016/j.matdes.2018.03.007.

[38] A.J. De Ardo, C.J. Simensen, A structural investigation of multiple aging of Al-7 wt pct Zn-2.3 wt pct Mg, Metall. Trans. 4 (1973) 2413–2421. https://doi.org/10.1007/BF02669384.

[39] V. Hansen, O.B. Karlsen, Y. Langsrud, J. Gjønnes, Precipitates, zones and transitions during aging of Al-Zn-Mg-Zr 7000 series alloy, Mater. Sci. Technol. 20 (2004) 185–193. https://doi.org/10.1179/026708304225010424.

[40] T.-F. Chung, Y.-L. Yang, B.-M. Huang, Z. Shi, J. Lin, T. Ohmura, J.-R. Yang, Transmission electron microscopy investigation of separated nucleation and in-situ nucleation in AA7050 aluminium alloy, Acta Mater. 149 (2018) 377–387. https://doi.org/10.1016/j.actamat.2018.02.045.

[41] T. Saito, C.D. Marioara, S.J. Andersen, W. Lefebvre, R. Holmestad, Aberration-corrected HAADF-STEM investigations of precipitate structures in Al-Mg-Si alloys with low Cu additions, Philos. Mag. 94 (2014) 520–531. https://doi.org/10.1080/14786435.2013.857051.

[42] J.K. Sunde, C.D. Marioara, A.T. van Helvoort, R. Holmestad, The evolution of precipitate crystal structures in an Al-Mg-Si(-Cu) alloy studied by a combined HAADF-STEM and SPED approach, Mater Charact 142 (2018) 458–469. https://doi.org/10.1016/j.matchar.2018.05.031.

[43] S.J. Andersen, C.D. Marioara, J. Friis, R. Bjørge, Q. Du, I. Ringdalen, S. Wenner, E.A. Mørtsell, R. Holmestad, T. Saito, J. Røyset, O. Reiso, Directionality and column arrangement principles of precipitates in Al-Mg-Si-(Cu) and Al-Mg-Cu linked to line defect in Al, Mater. Sci. Forum 877 (2016) 461–470. https://doi.org/10.4028/www.scientific.net/MSF.877.461.

[44] T. Saito, E.A. Mørtsell, S. Wenner, C.D. Marioara, S.J. Andersen, J. Friis, K. Matsuda, R. Holmestad, Atomic structures of precipitates in Al-Mg-Si alloys with small additions of other elements, Adv. Eng. Mater. 1800125 (2018) 1–18. https://doi.org/10.1002/adem.201800125.

[45] B. Milkereit, M.J. Starink, Quench sensitivity of Al-Mg-Si alloys: a model for linear cooling and strengthening, Mater. Des. 76 (2015) 117–129. https://doi.org/10.1016/j.matdes.2015.03.055.

[46] B. Milkereit, M. Österreich, P. Schuster, G. Kirov, E. Mukeli, O. Kessler, Dissolution and precipitation behavior for hot forming of 7021 and 7075 aluminum alloys, Metals 8 (2018) 531. https://doi.org/10.3390/met8070531.

[47] P. Schloth, J.N. Wagner, J.L. Fife, A. Menzel, J.M. Drezet, H. Van Swygenhoven, Early precipitation during cooling of an Al-Zn-Mg-Cu alloy revealed by in situ small angle X-ray scattering, Appl. Phys. Lett. 105 (2014) 9–12. https://doi.org/10.1063/1.4894768.

[48] P. Schumacher, S. Pogatscher, M.J. Starink, C. Schick, V. Mohles, B. Milkereit, Quench-induced precipitates in Al-Si alloys: calorimetric determination of solute content and characterisation of microstructure, Thermochim. Acta 602 (2015) 63–73. https://doi.org/10.1016/j.tca.2014.12.023.

[49] P. Schumacher, Plastisches Verformungsverhalten unterkühlter Aluminium-legierungen im System Al-Mg-Si,Ph.D. thesis. Universität Rostock. 2018.

[50] V. Hansen, A. Vevecka-Priftaj, J. Fjerdingen, Y. Langsrud, J. Gjønnes, The influence of silicon on age hardening kinetics and phase precipitations in Al-Mg-Zn alloys, Mater. Sci. Forum 519-521 (2006) 579–584. https://doi.org/10.4028/www.scientific.net/MSF.519-521.579.

[51] T. Saito, S. Wenner, E. Osmundsen, C.D. Marioara, S.J. Andersen, J. Røyset, W. Lefebvre, R. Holmestad, The effect of Zn on precipitation in Al-Mg-Si alloys, Philos. Mag. 94 (2014) 2410–2425. https://doi.org/10.1080/14786435.2014.913819.

[52] X.P. Ding, H. Cui, J.X. Zhang, H.X. Li, M.X. Guo, Z. Lin, L.Z. Zhuang, J.S. Zhang, The effect of Zn on the age hardening response in an Al-Mg-Si alloy, Mater. Des. 65 (2015) 1229–1235. https://doi.org/10.1016/j.matdes.2014.09.086.

[53] B.S. Gong, Z.J. Liu, Y.L. Wang, Z.J. Zhang, P. Zhang, H.C. Jiang, L.J. Rong, Z.F. Zhang, Improving the fatigue strength of A7N01 aluminum alloy by adjusting Si content, Mater. Sci. Eng. A 742 (2019) 15–22. https://doi.org/10.1016/j.msea.2018.10.085.

[54] H. She, W. Chu, D. Shu, J. Wang, B.-d. Sun, Effects of silicon content on microstructure and stress corrosion cracking resistance of 7050 aluminum alloy, Trans. Nonferrous Metals Soc. China 24 (2014) 2307–2313. https://doi.org/10.1016/S1003-6326(14)63349-5.

[55] H. Saitoh, Y. Iijima, K. Hirano, Behaviour of hydrogen in pure aluminium, Al-4 mass% Cu and Al-1 mass% Mg2Si alloys studied by tritium electron microautoradiography, J. Mater. Sci. 29 (1994) 5739–5744. https://doi.org/10.1007/BF00349974.

[56] X.Y. Sun, B. Zhang, H.Q. Lin, Y. Zhou, L. Sun, J.Q. Wang, E.H. Han, W. Ke, Atom probe tomographic study of elemental segregation at grain boundaries for a peak-aged Al-Zn-Mg alloy, Corros. Sci. 79 (2014) 1–4. https://doi.org/10.1016/j.corsci.2013.10.027.

[57] L. Oger, M.C. Lafouresse, G. Odemer, L. Peguet, C. Blanc, Hydrogen diffusion and trapping in a low copper 7xxx aluminium alloy investigated by Scanning Kelvin Probe Force Microscopy, Mater. Sci. Eng. A 706 (2017) 126–135. https://doi.org/10.1016/j.msea.2017.08.119.

[58] T. Tsuru, M. Yamaguchi, K. Ebihara, M. Itakura, Y. Shiihara, K. Matsuda, H. Toda, First-principles study of hydrogen segregation at the MgZn2 precipitate in Al-Mg-Zn alloys, Comput. Mater. Sci. 148 (2018) 301–306. https://doi.org/10.1016/j.commatsci.2018.03.009.